Journal

Phase Evolution in the Transformation of Atomically Mixed Versus Ball-Milled Mixtures of Nanopowders in the Formation of Composite MO·3Al₂O₃ Spinels: Bottom-Up Processing is Not Always Optimal

Nathan J. Taylor, Andrew J. Pottebaum, Veli Uz, and Richard M. Laine[†]

Department of Materials Science and Engineering, University of Michigan, Ann Arbor, Michigan 48109-2136

Liquid-feed flame spray pyrolysis (LF-FSP) provides atomically homogeneous mixed metal powders with 30–40 nm average particle sizes, often producing kinetic phases due to the high quench rate As produced LF-FSP Al_2O_3-rich spinels, such as $MgO \cdot 3Al_2O_3$, form an Al_2O_3-rich metastable single-phase spinel. On heating, the powders phase separate to form MAl_2O_4 and α-Al_2O_3. Compacts of $MO \cdot 3Al_2O_3$ (M = Co, Ni, Mg) were produced and sintered to evaluate the final duplex microstructure. The same composition was also approached from stoichiometric LF-FSP MAl_2O_4 nanopowders ball-milled with Al_2O_3 nanopowders in an attempt to evaluate how the initial length scale of mixing affected the final microstructure. Contrary to traditional sintering, we observe two distinct mechanisms. At 1000°C–1200°C, cation diffusion appears to control densification as a consequence of high vacancy concentrations and atomic mixing where traditionally expected site inversion plays less of a factor given the high quench rates. The second mechanism follows α-Al_2O_3 exsolution and densification occurs via oxygen diffusion and α-Al_2O_3 grain growth. When sintering the duplex MAl_2O_4/α-Al_2O_3 compacts to at least 95% theoretical density, we find final microstructures that do not reflect the initial degrees of mixing. That is, the atomically mixed $MgO \cdot 3Al_2O_3$ does not does not offer an advantage over the submicron length scale of mixing in the ball-milled samples.

I. Introduction

DEVELOPING a detailed understanding of diffusion processes is one of the most important facets in properties optimization in ceramics science and engineering. The opportunity to start from nano-oxide powders that are atomically mixed offers the potential to develop unique perspectives about these processes when sintering to produce dense monoliths. A further opportunity presents itself when the nanopowders have compositions outside traditional thermodynamic phase diagrams, as observed in liquid-feed flame spray pyrolysis (LF-FSP) nanopowders. Given that the powders are crystalline yet metastable, the potential exists to study phase-segregation without passing through chemically derived precursors that must be calcined prior to sintering, such as in sol–gel processing.

In two recent papers, we described studies along these lines designed to explore the concept of "bottom-up" processing in $Y_3Al_5O_{12}$ compositions made both from atomically mixed nanopowders and ball-milled mixtures of Y_2O_3 and Al_2O_3 nanopowders, and nanopowders with a final composition of $NiO \cdot 3Al_2O_3$.[1,2] Our findings were that the bottom-up concept

was either not the optimal route to the targeted materials with controlled microstructures or gave the same microstructures despite significant differences in levels of mixing.

The bottom-up concept, pervasive in materials science, suggests that the finest scales of mixing should provide the shortest diffusion paths, and therefore sintering times to fully dense materials with optimal control of final microstructures. In this study, we extend studies on the initial $NiO \cdot 3Al_2O_3$ system and now include two additional spinel systems with M = Mg and Co. Our objective here was to delineate microstructural and phase evolution in much greater detail than in the earlier study.

To this end, we have examined the sintering behavior of disordered MAl_2O_4/Al_2O_3 spinel solutions, in which the disorder gives rise to densification processes and rates different from that of the component systems, likely due to the high defect/vacancy contributions. In addition, we examine sintering of equivalent compositions from ball-milled powders to investigate the role of length scale of mixing in processing dense composites and its influence on control of final densities and microstructures.

$MgAl_2O_4$, $CoAl_2O_4$, and $NiAl_2O_4$ spinels are of significant technological interest for their inherent mechanical, optical, and catalytic properties.[3–10] Nanosized $MgAl_2O_4$, $CoAl_2O_4$, and $NiAl_2O_4$ spinel powders have been synthesized using a variety of methods including coprecipitation of metal hydroxides,[11,12] wet impregnation[12], sol–gel processing,[13] and spray pyrolysis.[14] High surface area (50 m²/g) spinel powders are of interest for both catalytic applications where surfaces exhibit high activity and sintering of ceramic monoliths in which reduction in surface area provides added driving force for densification.

Metal aluminate spinels having the general formula MAl_2O_4 are a class of materials with a wide range of properties dependent on the divalent cation. Metal aluminates belong to the cubic space group Fd3 m. The unit cell is composed of a pseudo-cubic closed packed oxygen lattice with 64 tetrahedral and 32 octahedral sites for divalent metal and aluminum cations. In normal spinel, 1/8 of the tetrahedral sites are filled by divalent atoms and 1/2 of the octahedral sites are occupied by aluminum atoms. In the unit cell of a fully inverted spinel, the aluminum atoms occupy 8 tetrahedral sites and 8 octahedral sites with the remaining 8 octahedral sites occupied by the divalent metal atoms.[15–17]

In metal aluminate spinels i, the inversion parameter, is defined as the fraction of tetrahedral sites occupied by aluminum atoms; thus it follows that in a normal spinel $i = 0$ and in a fully inverted spinel $i = 1$. In practice, the cation distribution is of a mixed nature with $0 < i < 1$, a function of the octahedral site preference energy (OSPE) of the constituent cations. The OSPE is a measure of the preference of a cationic species to be located on an octahedral site.[18,19]

The spinel structure consists of a rigid anion lattice through which cations diffuse.[20] Diffusional processes are dependent on the mobility of the divalent and trivalent

cations through the octahedral and tetrahedral sites formed by the oxygen lattice. From a mechanistic perspective, there are two major interactions to account for when considering cation diffusion. The lattice strain energy imposed by the diffusing cation and the preference of the diffusing cation to occupy a tetrahedral or octahedral site. Therefore, the mobility of a specific cation through the spinel oxygen lattice is a function of the cation radii and the OSPE of the cations.[21,22]

Liquid-feed flame spray pyrolysis offers access to a variety of metal and mixed metal oxide nanopowders over a wide range of ceramic systems. In LF-FSP, alcohol solutions of metalloorganic precursors are aerosolized with oxygen, combusted, and the resultant nanopowders are collected downstream in electrostatic precipitators.[23] Combustion produces oxide nanopowders with identical compositions to the precursor solution and high surface area powders due to a rapid quench from flame temperatures of 1200°C–2000°C to downstream temperatures of 300°C–400°C within nanoseconds. The resulting nanopowders are crystalline, have no microporosity, and offer good dispersability, with average particle sizes (APSs) of 15–40 nm.[24–30]

Previous work has shown that the high quench rate of LF-FSP provides routes to kinetic products. In the case of certain MO-Al_2O_3 [M = Mg, Co, Ni] systems, LF-FSP can produce single-phase MAl_2O_4 powders at Al_2O_3-rich compositions well outside the thermodynamically defined single-phase region.[14,27–29] The Al_2O_3-rich MAl_2O_4 materials are single-phase and can be considered a solid solution of the isostructural phases, γ-Al_2O_3 and MAl_2O_4.[31]

Here, we use single-phase MO·$3Al_2O_3$ powders to form Al_2O_3/MAl_2O_4 composites and compare the sintering behavior to ball-milled Al_2O_3 and MAl_2O_4 powders to investigate the effects of length scale of mixing on the sintering behavior of Al_2O_3/MAl_2O_4 composites. We then further examine the sintering behavior of the single-phase Al_2O_3-rich MAl_2O_4 powders in the context of the transition from a single-phase material to a duplex Al_2O_3/MAl_2O_4 composite.

II. Experimental Procedure

(1). Nanopowder Synthesis

Ni($O_2CH_2CH_3$)$_2$·$4H_2O$ was purchased from Sigma Aldrich (St. Louis, MO) and Mg(O_2CCH_3)$_2$·$4H_2O$ was purchased from Alfa Aesar (Ward Hill, MA) and used as received. Al(OCH_2CH_2)$_3$N was synthesized from Al($OsBu$)$_3$ and N(CH_2CH_2OH)$_3$ as described elsewhere.[31]

Co($O_2CCH_2CH_3$)$_2$ was synthesized by reaction of 200.0 g (1.46 mol) of CoCO$_3$·H_2O (Sigma Aldrich) in 500 mL (6.7 mol) $CH_3CH_2CO_2H$ (Sigma Aldrich) at 110°C for 6 h in a 1 L r/b flask with an N_2 sparge. The resulting solution was heated to 150°C for 2 h to distill off H_2O and excess $CH_3CH_2CO_2H$ after which Co($O_2CCH_2CH_3$)$_2$ was precipitated by addition of tetrahydrofuran. The resulting solid was filtered, air dried, and the ceramic yield was determined to be 31.3 wt% by thermogravimetric analysis (TGA).

Precursors were dissolved in anyhydrous ethanol (Decon Labs, King of Prussia, PA) and diluted to 3 wt% ceramic yield as measured by TGA. Powders were synthesized by LF-FSP, as detailed elsewhere,[25,26] in which precursor solutions are aerosolized and ignited using methane/O_2 pilot torches. Precursor combustion is followed by rapid quenching and the resultant powders are collected by electrostatic precipitation. Nanotek Al_2O_3 was received as a gift from Nanophase Technologies Corporation (Romeoville, IL).

(2). Pellet Processing

Approximately 30 g of as-produced MO·$3Al_2O_3$ [M = Mg, Co, or Ni] powder was added to 350 mL of ethanol with 2 wt % bicine (Sigma Aldrich) dispersant and ball-milled for 24 h using 3 mm 99% pure Al_2O_3 media. On removal of milling media, the suspension was ultrasonicated for 20 min at

100 W using a Vibracell VC 505 ultrasonicating horn (Sonics and Materials, Newton, CT). The suspension was allowed to settle for 24 h before decanting. The slurry was dried at 50°C.

Dried powder was ground in an agate mortar and sieved through a 75 μm polymer mesh, dispersed in ethanol with 4 wt% PEG 3400 (Sigma Aldrich) as binder and dried. Dried powder was sieved through a 20 μm polymer mesh. Samples (500 mg) were weighed out and uniaxially pressed into pellets at 14 MPa. Uniaxially pressed pellets were CIPped (Autoclave Engineers Inc., Erie, PA) to 200 MPa and held at pressure for 30 min. Ball-milled MAl_2O_4 + Al_2O_3 pellets were produced under identical conditions except that the component powders, LF-FSP MAl_2O_4 [M = Mg, Co, or Ni] and Nanotek Al_2O_3 were settled before ball-milling to ensure correct stoichiometry upon mixing.

(3). Burnout and Sintering

Pellets were burned out at 500°C (ramp rate of 3°C/min) for 4 h in flowing O_2 (50 mL/min) to remove residual organics. Pellets and powders were sintered in a MTI GSL-1600X tube furnace (MTI Corp., Richmond, CA) under flowing dry air (50 mL/min). Sintering ramp rates were 10°C/min below 1100°C and 5°C/min above 1100°C.

(4). Analytical Techniques

(A). Specific Surface Areas: Specific surface area (SSA) measurements were run on an ASAP 2020 (Micromeritics Inc., Norcross, GA). Powder samples (400 mg) were degassed at 400°C under vacuum for 8 h and a 10-point analysis was conducted at 77 K in liquid N_2 over a relative pressure range of 0.05–0.35 p/p$_o$. SSAs were determined using the Brunauer–Emmett–Teller (BET) method and APSs (<R>) were calculated using the formula $<R> = \frac{6000}{\rho(SSA)}$ where ρ is the density of the material in g/cm^3.

(B). X-Ray Diffraction: X-ray diffraction (XRD) patterns were obtained using a Rigaku high-intensity rotating anode diffractometer (Rigaku, The Woodlands, TX) with a copper target ($\lambda = 1.54$ Å), a graphite diffracted beam monochromator, and a working voltage and current of 40 kV and 100 mA, respectively. Powder samples were prepared by packing ~100 mg of powder into an amorphous silica holder. Pellets were mounted to face the source on a metal sample holder. Scans were continuous from 10 to 70° 2θ in 0.02° increments.

Phase identification was carried out by comparison with standard materials: α-Al_2O_3 (PDF File#: 00-010-0173), CoAl$_2O_4$ (PDF File#: 00-044-0160), MgAl$_2O_4$ (PDF File#: 00-021-1152), NiAl$_2O_4$ (PDF File#: 01-071-0964), and NiAl$_{10}O_{16}$ (PDF File#: 00-037-1292). Vegards law calculations were run using an internal Si (111) standard. Lattice constants were determined from the (400) peak of each pattern using 0.7900 Å as the lattice parameter for γ-Al_2O_4, 8.0831 Å as the lattice parameter for MgAl$_2O_4$, 8.1040 Å as the lattice parameter for CoAl$_2O_4$, and 8.0531 Å as the lattice parameter for NiAl$_2O_4$. Phase relations were characterized by Rietveld refinements using Jade 10 (Materials Data Inc., Livermore, CA) and a 2-point linear background.

(C). TGA—Differential Thermal Analysis (TGA-DTA): Thermogravimetric analysis—differential thermal analysis (TGA-DTA) was performed using a Q600 TGA-DTA instrument (TA Instruments Inc., New Castle, DE). About 15–30 mg samples were pressed in a 3 mm die and placed in an alumina pan. Samples were heated to 1400°C at a ramp rate of 10°C/min in dry air (60 mL/min). An α-alumina reference pan was used as a thermal reference.

(5). Dilatometry

Dilatometry measurements were taken using a Theta Industries Dilatronic II (Port Washington, NY) equipped with a

single push-rod loading dilatometry setup. Square samples were cut from 12.7 mm diameter pellets (pellet processing described above). Experiments were run in static air at a constant heating rate of 10°C/min to 1500°C.

(A). Scanning Electron Microscopy: Scanning electron microscopy (SEM) was performed using a FEI Nova Nanolab dualbeam SEM/FIB (FEI Corporation, Hillsboro, OR). Pellets were ground and polished with a water rinse between each step. Polished samples were thermally etched for 1 h at a temperature 100°C below the final sintering temperature. Samples were sputter coated with Au-Pd using a Technics Himmer VI sputtering system (Anatech Ltd., Alexandria, VA) to reduce charging.

III. Results and Discussion

As noted above, we are interested in the microstructural evolution of $MO\cdot 3Al_2O_3$ (M = Mg, Co, and Ni) using nanopowders that offer a homogeneous composition at atomic length scales versus, mixtures of nanopowders of the same composition but with homogeneity defined by ball-milling of the same ratios of the two component nanooxide powders.[1,2] In all instances, the nanopowders used offer APSs of ≈30–40 nm. In the latter case, we believe that the homogeneity of mixing is submicron rather that atomic. Our goal has been to explore the potential utility of the "bottom up" synthesis paradigm to processing of bulk ceramics from nanopowders.[32]

Starting powders were synthesized by LF-FSP which provides a route to both atomically mixed, single-phase Al_2O_3-rich MAl_2O_4 [M = Mg, Co, Ni], hereafter referred to as $NiO\cdot 3Al_2O_3$, and stoichiometric MAl_2O_4 which was ball-milled with Al_2O_3 to produce materials of equivalent composition, hereafter referred to as $MAl_2O_4 + Al_2O_3$.

(1). Powder Characterization

SEM was performed on all as-produced powders to assess the homogeneity of particle sizes and determine the particle morphologies. Powders were agglomerated due to electrostatic interactions but contained no micron-sized particles. The particles appeared largely homogenous in terms of particle size and spherical morphology. Figure 1 shows as-produced $MgO\cdot 3Al_2O_3$ powders, representative of all LF-FSP materials produced in this study.

Table I presents SSAs of the as-produced powders. No hysteresis was observed in the BET adsorption/desorption isotherms indicating that the particles had no surface porosity.
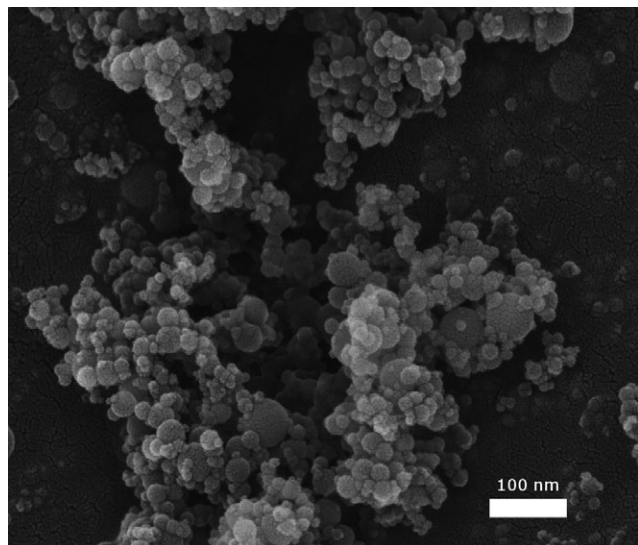

Fig. 1. Scanning electron microscopy micrograph of $MgO\cdot 3Al_2O_3$.

Table I. BET Results of Starting Powders

Powder	Density (g/cm³)	SSA (±1 m²/g)	APS (±2 nm)
$MgO\cdot 3Al_2O_3$	3.74	51	31
$CoO\cdot 3Al_2O_3$	4.25	42	34
$NiO\cdot 3Al_2O_3$	4.29	43	33
$MgAl_2O_4$	3.59	38	44
$CoAl_2O_4$	4.42	48	28
$NiAl_2O_4$	4.49	41	33
Nanotek Al_2O_3	3.6	30	56

BET, Brunauer–Emmett–Teller; SSA, specific surface area; APS, average particle size.

Figure 2 shows powder XRD patterns for as-produced $MO\cdot 3Al_2O_3$ powders. As-produced powders are single phase and can be considered solid solutions of γ-Al_2O_3 and MAl_2O_4 as γ-Al_2O_3 has a defect spinel structure.[33,34] XRD patterns taken with Si (111) standards were used to determine the lattice parameters of the as-produced powders. The lattice parameters were found to be 7.99 Å for $MgO\cdot 3Al_2O_3$, 8.01 Å for $CoO\cdot 3Al_2O_3$, and 7.98 Å for $NiO\cdot 3Al_2O_3$, which correspond to points at 48% along the Al_2O_3-$MgAl_2O_4$ tie line, 54% along the Al_2O_3-$CoAl_2O_4$ tie line, and 51% along the Al_2O_3-$NiAl_2O_4$ tie line. The powders are generally in good agreement with the predicted lattice parameter as determined by Vegard's law of a 1:1 solid solution of γ-Al_2O_3 and MAl_2O_4.

Although the deviations from Vegard's law are less than ±4%, there is evidence to suggest that the spinel inversion parameter can affect the lattice parameter in $MgAl_2O_4$.[35] Given the kinetic nature of particle formation in LF-FSP, the $MgAl_2O_4$ may have significantly higher inversion than the spinel synthesized by other methods. The deviation from Vegard's law could also arise from small stoichiometry deviations due to inhomogeneous precursors.

(2). Final Microstructures

Samples of $MO\cdot 3Al_2O_3$ and $MAl_2O_4 + Al_2O_3$ were subjected to two sintering schedules both targeting practical densities of ≥95% of theoretical density (TD) in all materials. The low temperature schedule (LT) with holds at 1150°C–4 h, 1300°C–8 h, and 1400°C–4 h was intended to minimize grain growth during densification. The results are compared with a high-temperature schedule (HT) comprised of a single hold at 1400°C for 10 h. All sintering was performed in air as initial studies under O_2, N_2, and vacuum were found to have no effect on densification behavior. Figure 3 shows microstructures for $MgO\cdot 3Al_2O_3$ and $MgAl_2O_4 + Al_2O_3$ sintered at the HT and LT schedules. These microstructures are typical of all three systems studied. Figures S1–S3 show microstructures for the magnesium, cobalt, and nickel systems.

Average grain sizes (AGSs) were measured by the lineal intercept method. Included in the grain size plots of Figs. 4–6 are the 95% confidence interval (box) and variance (bars) of measurements taken for each sample.

With the exception of the ball-milled $NiAl_2O_4 + Al_2O_3$ samples, the lower temperature sintering schedule reduces the AGS by 240 ±150 nm. However, the differences between the AGSs of the LT and HT samples are within the 95% confidence interval. Thus, the size difference is not statistically significant except in the case of the $MgO\cdot 3Al_2O_3$, where the single, high-temperature sintering step results in grain sizes significantly larger than that of the low temperature sintering schedule. In this case, the high-temperature sintering step may be above a temperature at which significant grain coarsening occurs.

Surprisingly, samples made from the ball-milled $MAl_2O_4 + Al_2O_3$ powders produce compacts with AGSs equivalent to samples made from the atomically mixed $MO\cdot 3Al_2O_3$ powder. This finding implies that mixing of
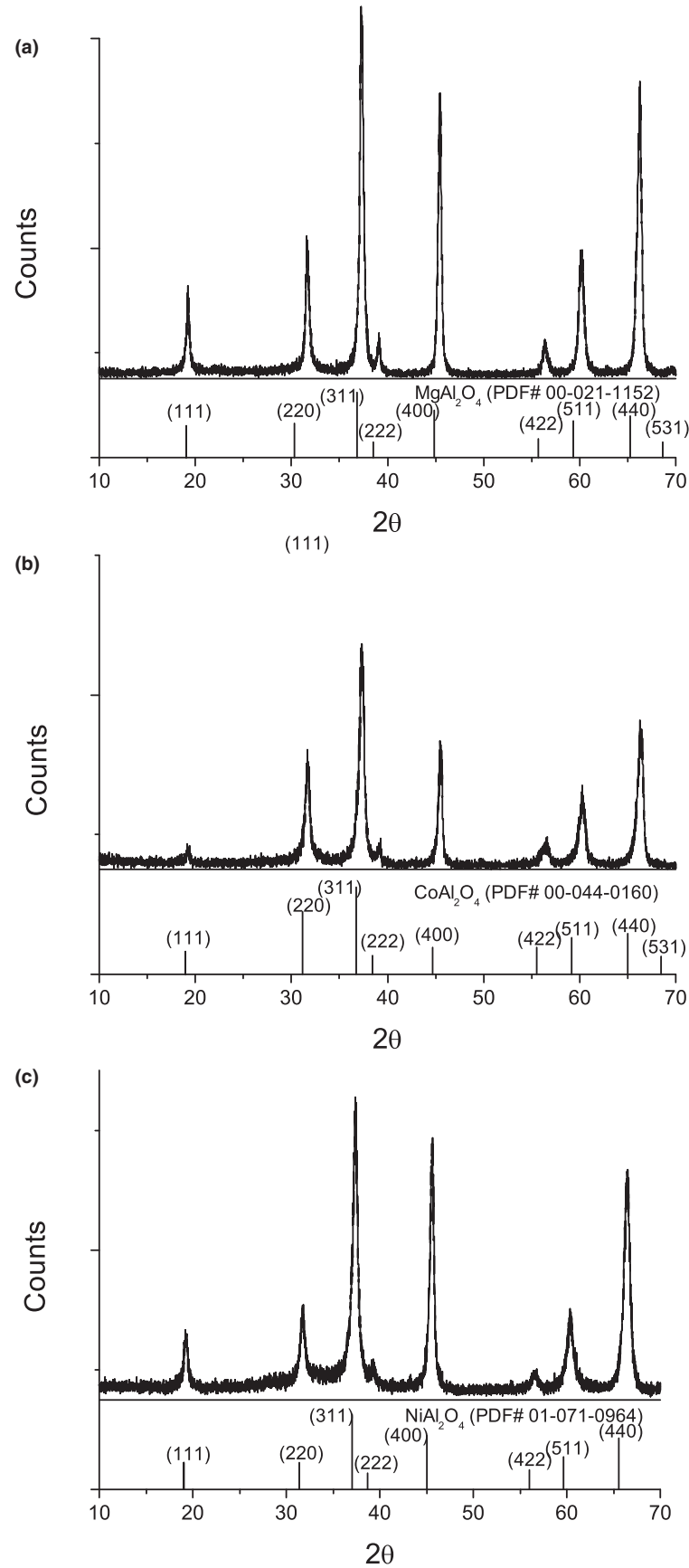
Fig. 2. X-ray diffraction patterns of as-produced MO·3Al₂O₃ powder with PDF for (a) MgO·3Al₂O₃ (b) CoO·3Al₂O₃ (c) NiO·3Al₂O₃.

constituent powders at atomic length scales does not correspond to finer grain sizes in the final microstructures of dense composites when compared to mixing at nanometer length scales. This observation seems counter to the widely accepted bottom-up approach to processing that has been widely accepted throughout the literature.[33]
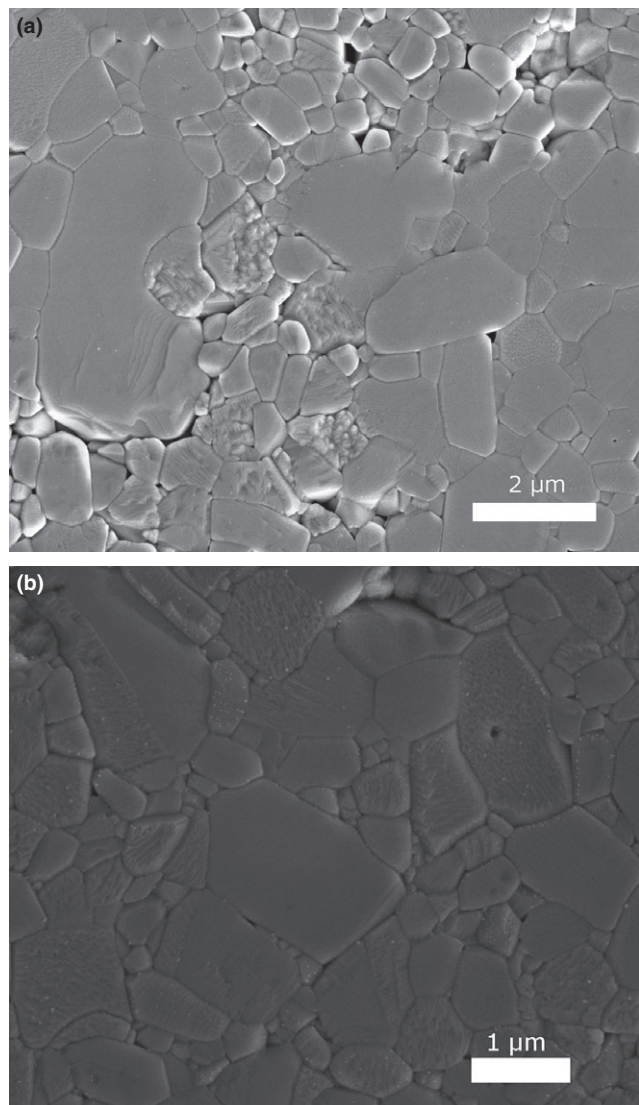
Fig. 3. Scanning electron microscopy micrographs of polished $MgAl_2O_4$ pellets (a) $MgO \cdot 3Al_2O_3$ high-temperature (HT) (b) $MgAl_2O_4 + Al_2O_3$ HT.

(3). Phase Exsolution and Sintering Behavior

The effects of exsolution on the sintering behavior of $MO \cdot 3Al_2O_3$ compacts were investigated by combined dilatometry and XRD studies of powders heated at 10°C/min/air to selected temperatures with a 1 h dwell. The ramp rate for heating of all XRD samples was 10°C/min.

Figures 7 and 8 present XRD and dilatometry data for $CoO \cdot 3Al_2O_3$ and $MgO \cdot 3Al_2O_3$, respectively. Here, we observe α-Al_2O_3 and MAl_2O_4 [M = Mg and Co] exsolution directly from the as-produced Al_2O_3-rich MAl_2O_4. Dilatometry curves for these two materials indicate similar, two stage, sintering behavior with the onset of densification for the $CoO \cdot 3Al_2O_3$ and $MgO \cdot 3Al_2O_3$ at 1050°C and 1160°C, respectively. In both systems, considerable densification, approximately 20% TD by dilatometry, occurs prior to exsolution of α-Al_2O_3, and the densification rate slows significantly coincident with exsolution. It is likely that the α-Al_2O_3 greatly slows sintering following exsolution, either through slower sintering kinetics or by presenting a physical barrier. A similar enhancement in densification in Al_2O_3-rich spinels was seen by Krell *et al.*[36] in which sintering of $MgO \cdot nAl_2O_3$ was promoted in samples where $n > 1.5$, although $n = 3.0$ in this study, represents a significantly higher Al_2O_3 content.

Figure 9 shows the XRD and dilatometry for $NiO \cdot 3Al_2O_3$. In the case of $NiO \cdot 3Al_2O_3$, an intermediate phase, $NiAl_{10}O_{16}$, forms prior to separation of α-Al_2O_3 and $NiAl_2O_4$. Bassoul and Gilles report that $NiAl_{10}O_{16}$ is monoclinic and exhibits a periodic antiphase boundary structure based on the $(100)_c$ plane of the $NiAl_2O_4$ structure.[37,38] Here, we observe conversion of $NiO \cdot 3Al_2O_3$ to $NiAl_{10}O_{16}$ before phase separation of α-Al_2O_3 and, unlike the cobalt and magnesium systems, phase separation of Al_2O_3 does not immediately hinder densification, as seen in the combined dilatometry/XRD plots. The $NiAl_{10}O_{16}$ phase is Ni deficient compared to the original $NiO \cdot 3Al_2O_3$ composition, meaning the remaining spinel phase must be Ni rich. The conversion of the $NiO \cdot 3Al_2O_3$ material to $NiAl_{10}O_{16}$ is likely why densification continues after α-Al_2O_3 nucleates, in contrast to the cobalt and magnesium systems, where densification is slowed. To our knowledge, the sintering behavior of the metastable $NiAl_{10}O_{16}$ has not been studied.

Although the $NiAl_{10}O_{16}$ was previously described by Bassoul and Gilles, relatively few studies on this phase exist because it is difficult to access except in bulk. The work reported here, offers, for the first time, simple access to this phase from nanopowders, which may allow future researchers to explore their properties including for example, catalytic behavior.

Table II contains the dilatometry results for the first densification regime across all three systems. The $CoO \cdot 3Al_2O_3$ shows the lowest amount of densification in the initial densification regime, approximately 20% TD. The dilatometry trace for $MgO \cdot 3Al_2O_3$ is similar to that of the $CoO \cdot 3Al_2O_3$,
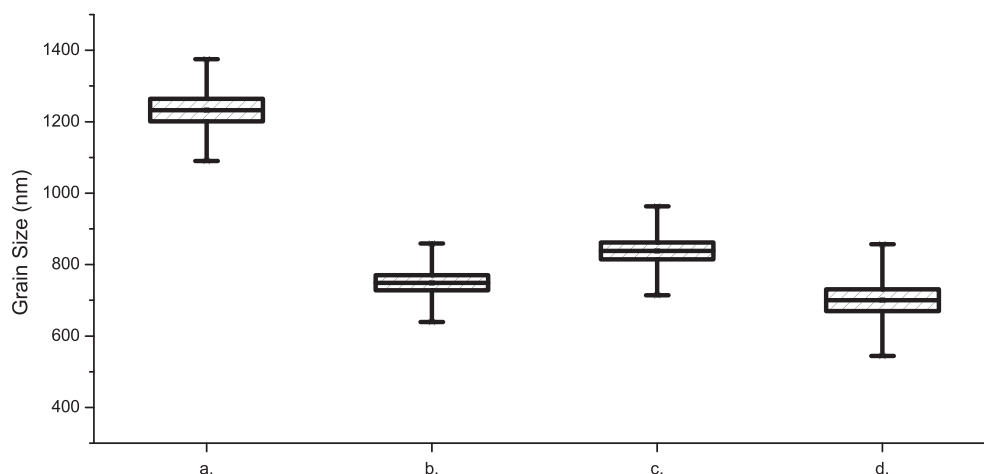
Fig. 4. Grain sizes of Al_2O_3–$MgAl_2O_4$ composites (a) $MgO \cdot 3Al_2O_3$ high-temperature (HT) (b) $MgO \cdot 3Al_2O_3$ low-temperature (LT) (c) $MgAl_2O_4 + Al_2O_3$ HT (d) $MgAl_2O_4 + Al_2O_3$ LT.
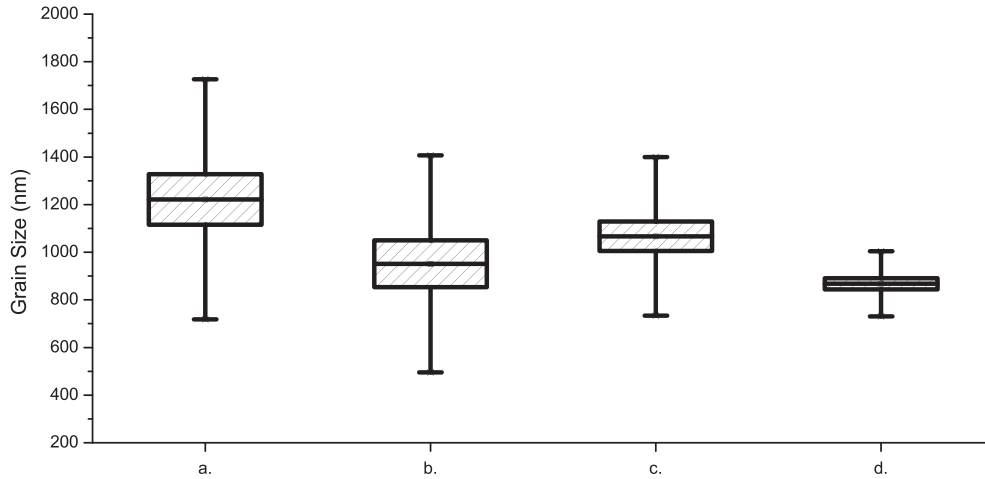
Fig. 5. Grain sizes of Al_2O_3–$CoAl_2O_4$ composites (a) $CoO·3Al_2O_3$ high-temperature (HT) (b) $CoO·3Al_2O_3$ low-temperature (LT) (c) $CoAl_2O_4 + Al_2O_3$ HT (d) $CoAl_2O_4 + Al_2O_3$ LT.
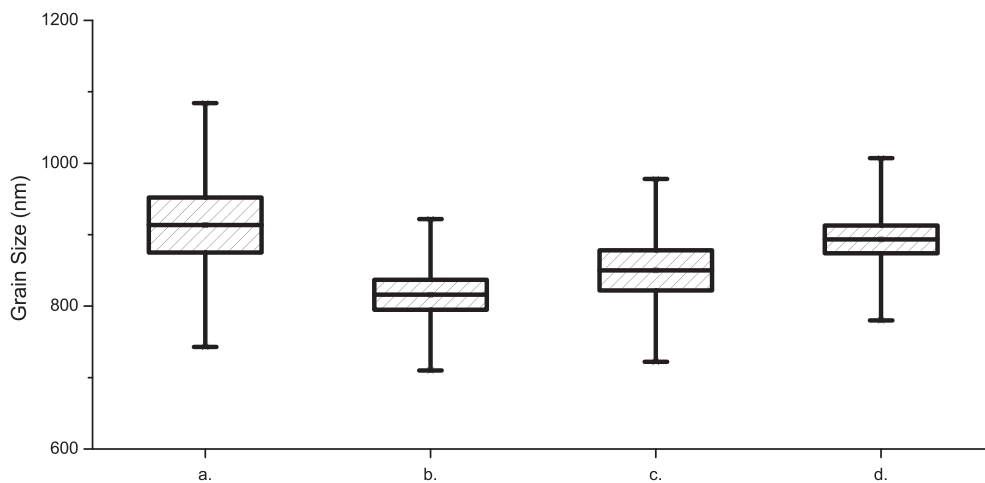
Fig. 6. Grain sizes of Al_2O_3–$NiAl_2O_4$ composites (a) $NiO·3Al_2O_3$ high-temperature (HT) (b) $NiO·3Al_2O_3$ low-temperature (LT) (c) $NiAl_2O_4 + Al_2O_3$ HT (d) $NiAl_2O_4 + Al_2O_3$ LT.
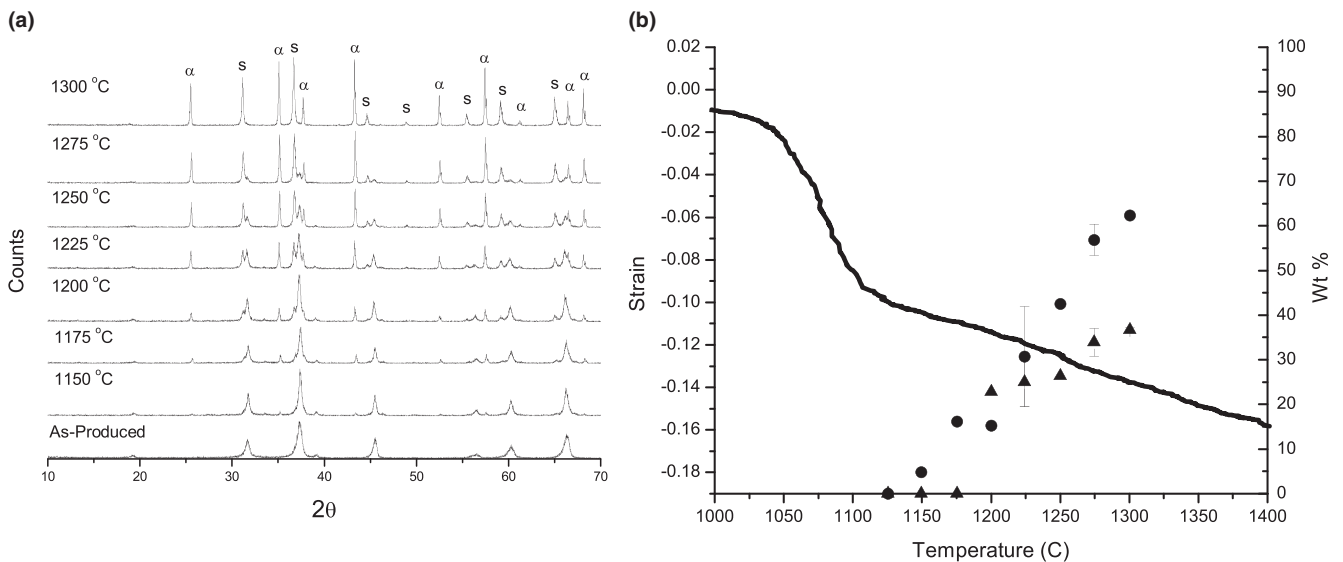
Fig. 7. (a) X-ray diffraction (XRD) results of phase separation of α-Al_2O_3 (α) and $CoAl_2O_4$ (S) from $CoO·3Al_2O_3$ powders heated for 1 h. (b) $CoO·3Al_2O_3$ dilatometry results plotted with amount of α-Al_2O_3 (•) and $CoAl_2O_4$ (▲) from XRD patterns of powders heated for 1 h.

but shows approximately 24% TD densification. As previously discussed, the $NiO·3Al_2O_3$ does not densify until after exsolution begins, with approximately 33% TD densification during the initial densification regime.

In a previously published study on $NiO·3Al_2O_3$, we looked at the degree of mixing of the starting materials versus the final microstructure and densities.[2] The current study represents a more in depth look at the sintering behavior of
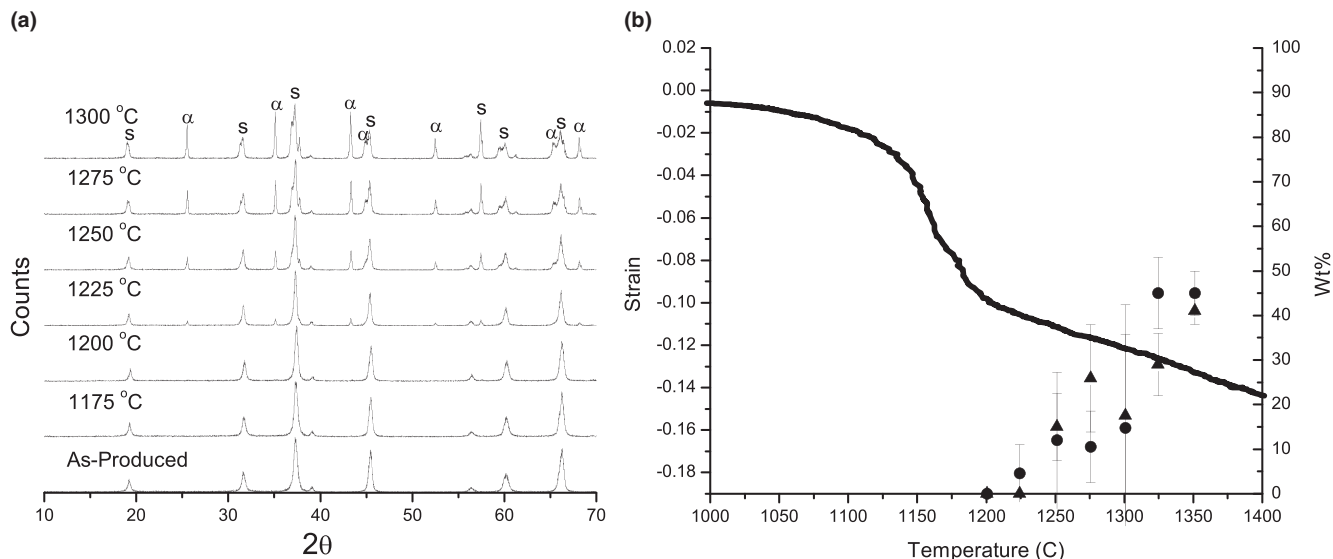
Fig. 8. (a) X-ray diffraction (XRD) results of phase separation of α-Al_2O_3 (α) and $MgAl_2O_4$ (S) from $MgO \cdot 3Al_2O_3$ powders heated for 1 h. (b) $MgO \cdot 3Al_2O_3$ dilatometry results plotted with amount of α-Al_2O_3 (•) and $MgAl_2O_4$ (▲) from XRD patterns of powders heated for 1 h.
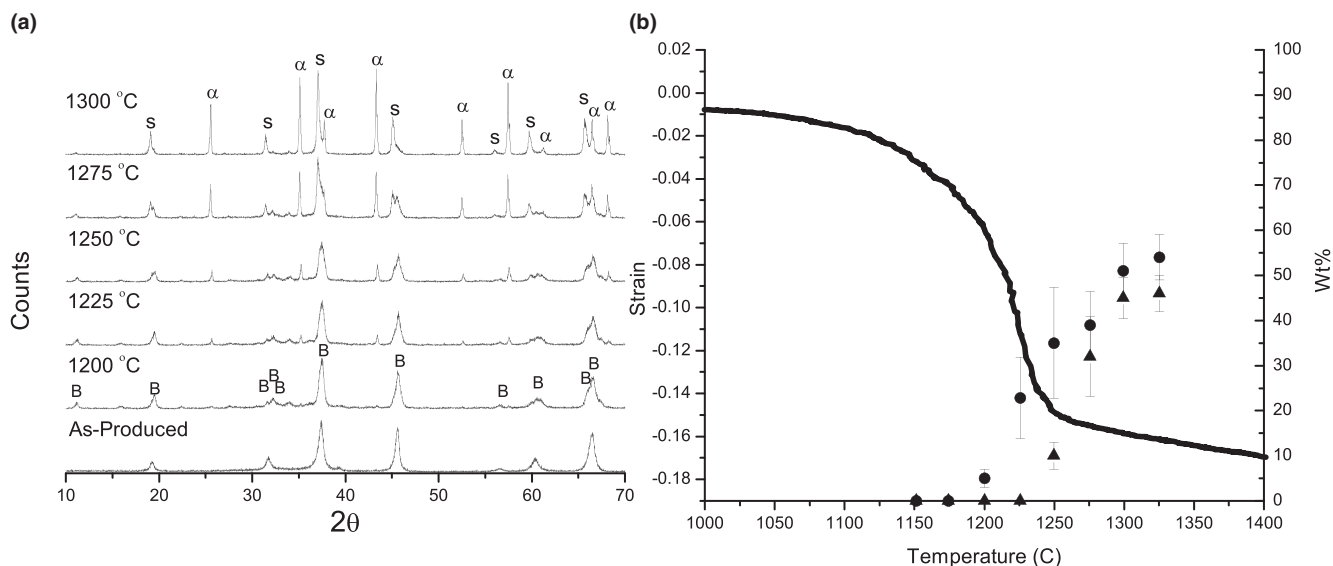
Fig. 9. (a) X-ray diffraction (XRD) results of phase separation of $NiAl_{10}O_{16}$ (B), α-Al_2O_3 (α) and $NiAl_2O_4$ (S) from $NiO \cdot 3Al_2O_3$ for powders heated for 1 h. (b) $NiO \cdot 3Al_2O_3$ dilatometry results plotted with amount of α-Al_2O_3 (•) and $NiAl_2O_4$ (▲) from XRD patterns from powders heated for 1 h.

Table II. Instantaneous Densities (% Theoretical Density) During Dilatometry

	$MgO \cdot 3Al_2O_3$	$CoO \cdot 3Al_2O_3$	$NiO \cdot 3Al_2O_3$
Green density (%)	55	56	53
Apparent exsolution onset temperature (°C)	1150	1050	1200
After first regime (%)	79	76	86
At 1400°C (%)	87	93	93

$NiO \cdot 3Al_2O_3$ throughout the exsolution process, which is shown by dilatometry to differ from that of the $MgO \cdot 3Al_2O_3$ and $CoO \cdot 3Al_2O_3$ systems.

Diffusion in stoichiometric spinels is governed by oxygen mobility, which is reported to be several orders of magnitude smaller than the cation mobility.[39,40] However, the kinetic nature of the as-produced $MO \cdot 3Al_2O_3$ powders necessitates rearrangement of the cations to form the thermodynamically

favored α-Al_2O_3/MAl_2O_4 composite. The as-produced powders likely deviate from the thermodynamically favored inversion levels due to the rapid quenching of LF-FSP. Since astoichiometry in Al_2O_3-rich spinels creates 1/8 cation vacancy per additional Al,[41,42] the Al_2O_3-rich materials studied here have a high number of cation vacancies. The role of cation vacancies in altering the densification behavior of these materials was investigated by comparing dilatometry curves of the component oxides, Al_2O_3 and MAl_2O_4, with the Al_2O_3-rich $MO \cdot 3Al_2O_3$, materials (Fig. 10).

The dilatometry results indicate that the initial onset of densification scales with the onset of densification for the respective stoichiometric MAl_2O_4. This is most pronounced in the cobalt system where we observe sintering of the $CoAl_2O_4$ at just above 900°C and a much earlier onset of densification, 1050°C, for $CoO \cdot 3Al_2O_3$ when compared to 1130°C and 1160°C for $NiO \cdot 3Al_2O_3$ and $MgO \cdot 3Al_2O_3$, respectively.

Comparison of the densification behavior of Nanotek 70:30 δ/γ-Al_2O_3 with those of the $MO \cdot 3Al_2O_3$ materials seems to
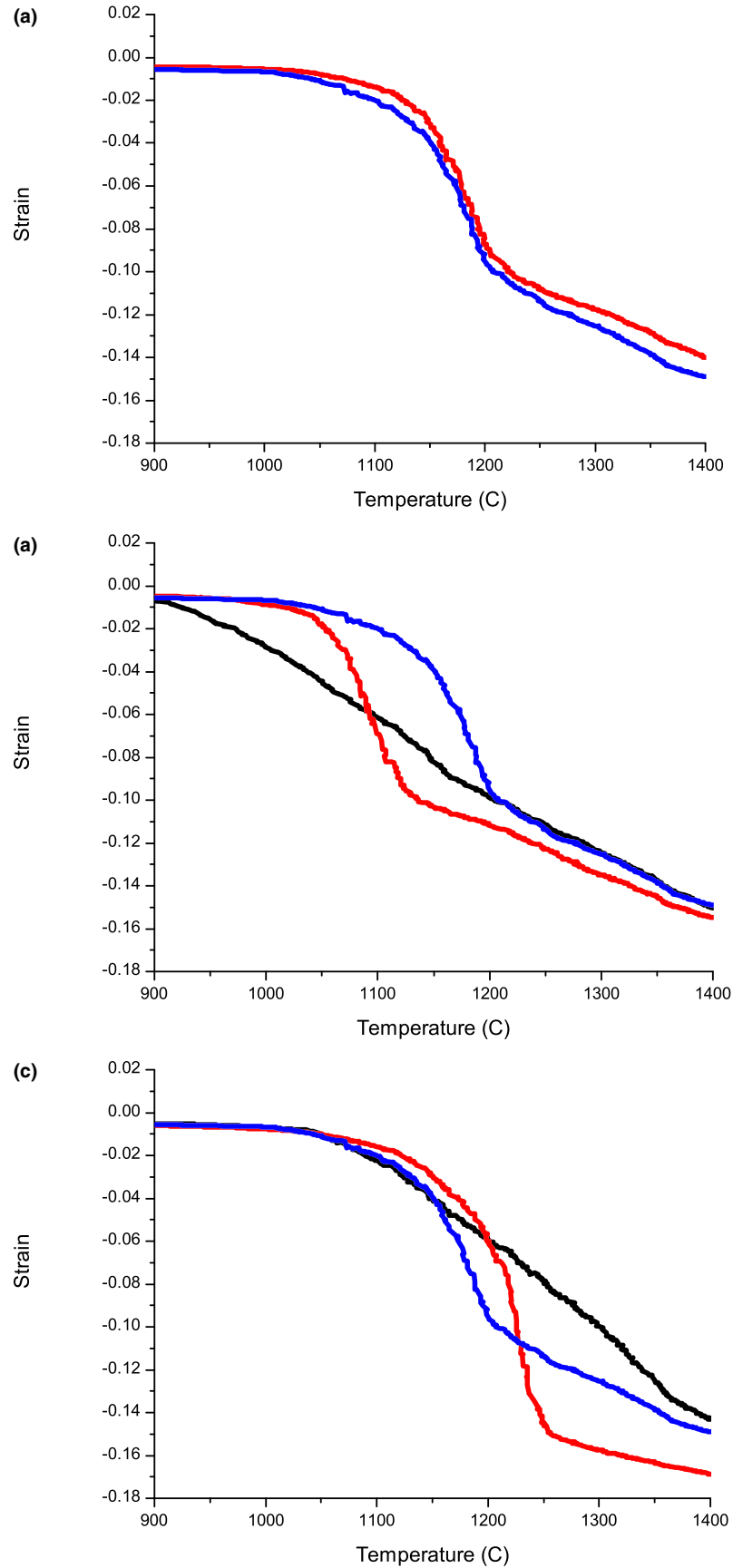
(a)

(a)

(c)

Fig. 10. Dilatometry curves of Al_2O_3 (blue) and MAl_2O_4 (black), and $MO \cdot 3Al_2O_3$ (red) for (a) M = Mg (b) M = Co and (c) M = Ni.

indicate that part of the initially enhanced densification, the first densification regime, in the $MO \cdot 3Al_2O_3$ materials could arise due to the γ-Al_2O_3 to α-Al_2O_3 transformation. In the

Nanotek δ/γ-Al_2O_3, the steep initial densification regime shown in blue in Figure 10 coincides with the γ-Al_2O_3 to α-Al_2O_3 phase transformation. The -0.06 linear strain in this

densification region is larger than theory for the transformation, -0.034, indicating some densification coincides with the transformation. However, since XRD studies of the magnesium and cobalt materials do not show α-Al_2O_3 until after the as-produced powders enter the second densification regime, we argue that the first densification regime in these systems is likely a result of cation rearrangement in the $MO \cdot 3Al_2O_3$, enhanced by the high concentration of cation vacancies.

Given only that the Al_2O_3 content of the three materials is the same, the cation vacancy concentration should be similar between these materials, however, the octahedral site preference of the divalent cation varies between the three materials such that $Ni > Co > Mg$ implying an increasing degree of inversion between the materials studied such that $MgO \cdot 3Al_2O_3 < CoO \cdot 3Al_2O_3 < NiO \cdot 3Al_2O_3$.[43–45] In this context, the earlier onset of densification in $CoO \cdot 3Al_2O_3$ when compared to $MgO \cdot 3Al_2O_3$ may be explained by the lower octahedral site preference of Co, allowing for a greater number of lattice sites to participate in diffusion.

This process is enhanced by a relatively higher concentration of cation vacancies in these Al_2O_3-rich materials when compared to their stoichiometric counterparts. Dilatometry shows the formation of the $NiAl_{10}O_{16}$ phase appears to retard densification onset but leads to significant densification during exsolution in contrast to the other two systems.

Diffusion of cations during exsolution eventually leads to regions rich in the divalent cations, promoting nucleation of α-Al_2O_3. The $NiO \cdot 3Al_2O_3$ material densifies approximately 33% TD compared to the initial 20% TD densification for $CoO \cdot 3Al_2O_3$ and $MgO \cdot 3Al_2O_3$ materials which is accompanied by the appearance of α-Al_2O_3 in the XRD studies. We attribute the defect-rich intermediate $NiAl_{10}O_{16}$ phase to the anomalous sintering behavior that allows for rapid diffusion in the first densification regime beyond the point at which we observe nucleation of α-Al_2O_3.

The sharp reduction in densification rate in the second regime for each of the $MO \cdot 3Al_2O_3$ materials can be interpreted as a shift in the densification rate-limiting species from cations to oxygen anions, the rate-limiting species in α-Al_2O_3. Once the $MO \cdot 3Al_2O_3$ materials precipitate MAl_2O_4 and α-Al_2O_3, diffusional processes are dominated by oxygen mobility and the rate of densification is slowed.

To clarify, each $MO \cdot 3Al_2O_3$ shows a similar initial densification regime not seen in the corresponding phase pure spinels. For the $MgO \cdot 3Al_2O_3$ and $CoO \cdot 3Al_2O_3$ systems, this densification regime happens prior to exsolution of α-Al_2O_3. For $NiO \cdot 3Al_2O_3$, an intermediate $NiAl_{10}O_{16}$ phase forms, and the initial densification regime is concomitant with α-Al_2O_3 exsolution. The cause of the initial densification regime is not immediately clear, and may arise due to a number of factors. The first being the high number of cation vacancies necessarily present in the Al_2O_3-rich spinel. In addition, the highly kinetic LF-FSP synthesis process may introduce further defects that drive this densification process. The kinetic nature of the synthesis process may also provide spinels with inversion levels different from the thermodynamically favored inversion level. The rearrangement of cations to the thermodynamically favored inversion level may facilitate densification.

IV. Conclusions

Al_2O_3-rich MAl_2O_3 [M = Ni, Co, Mg] single-phase nanopowders were produced by LF-FSP at the composition of $MO \cdot 3Al_2O_3$. Upon heating, the powders phase separate to α-Al_2O_3 and MAl_2O_3. Compacts of the $MO \cdot 3Al_2O_3$ powders were produced that resulted in dense α-Al_2O_3/MAl_2O_4 composites after sintering. Compacts of the same composition were prepared by ball-milling MAl_2O_4 and Al_2O_3 nanopowders. Despite the difference in initial length scales of compositional mixing, both routes produce microstructures with AGSs that are not statistically different.

Through a combined dilatometry and XRD study, we establish that in the Mg and Co systems, densification occurs prior to nucleation of α-Al_2O_3 from the solid solution phase. We attribute the initial densification to cation rearrangement in the solid solution. Once α-Al_2O_3 is nucleated, densification is slowed. In the $NiO \cdot 3Al_2O_3$ system, the solid solution transforms to a metastable $NiAl_{10}O_{16}$ phase. The $NiAl_{10}O_{16}$ phase then densifies while retarding the nucleation of α-Al_2O_3.

In the Mg and Co systems, an initial densification region is present by dilatometry that does not appear in the stoichiometric spinel dilatometry. We attribute this densification region to a combination of rearrangement of the cations in the highly disordered Al_2O_3-rich spinel lattice and the corresponding density increases upon transformation to α-Al_2O_3. In the Ni system, this densification regime is delayed until the intermediate $NiAl_{10}O_{16}$ phase transforms to α-Al_2O_3.

Supporting Information

Additional Supporting Information may be found in the online version of this article:

Fig. S1. SEM micrographs of polished $MgAl_2O_4$ pellets (a) $MgO \cdot 3Al_2O_3$ HT (b) $MgO \cdot 3Al_2O_3$ LT (c) $MgAl_2O_4$ + Al_2O_3 HT (d) $MgAl_2O_4$ + Al_2O_3 LT.

Fig. S2. SEM micrographs of polished $CoAl_2O_4$ pellets (a) $CoO \cdot 3Al_2O_3$ HT (b) $CoO \cdot 3Al_2O_3$ LT (c) $CoAl_2O_4$ + Al_2O_3 HT (d) $CoAl_2O_4$ + Al_2O_3 LT.

Fig. S3. SEM micrographs of polished $NiAl_2O_4$ pellets (a) $NiO \cdot 3Al_2O_3$ HT (b) $NiO \cdot 3Al_2O_3$ LT (c) $NiAl_2O_4$ + Al_2O_3 HT (d) $NiAl_2O_4$ + Al_2O_3 LT.

References

[1]N. J. Taylor and R. M. Laine, "Extrusion of YAG Tubes Shows Bottom-up Processing is not Always Optimal," *Adv. Func. Mater.*, **24** [8] 1125–32 (2014).

[2]N. J. Taylor, A. J. Pottebaum, V. Uz, and R. M. Laine, "The Bottom up Approach is not Always the Best Processing Method: Dense α-Al2O3/NiAl2O4 Composites," *Adv. Func. Mater.*, **24** [22] 3392–8 (2014).

[3]C. Otero Areán, M. Peñarroya Mentruit, A. J. López López, and J. B. Parra, "High Surface Area Nickel Aluminate Spinels Prepared by a Sol-Gel Method," *Colloids Surf. A Physicochem. Eng. Asp.*, **180**, 253–8 (2001).

[4]J. R. H. Ross, M. C. F. Steel, and A. Zeini-Isfahani, "Evidence for the Participation of Nickel Aluminate Sites in Steam Reforming of Methane over Nickel/Alumina Catalysts," *J. Catal.*, **52**, 280–90 (1978).

[5]Z. Chen, E. Shi, W. Li, Y. Zheng, and W. Zhong, "Hydrothermal Synthesis and Optical Property of Nano-Sized CoAl2O4 Pigment," *Mater. Lett.*, **55**, 281–4 (2002).

[6]W.-S. Cho and M. Kakihana, "Crystallization of Ceramic Pigment CoAl2O4 Nanocrystals from Co-Al Metal Organic Precursor," *J. Alloys Compd.*, **287** [1–2] 87–90 (1999)

[7]A. Sirijaruphan, A. Horváth, J. G. GoodwinJr, and R. Oukaci, "Cobalt Aluminate Formation in Alumina-Supported Cobalt Catalysts: Effects of Cobalt Reduction State and Water Vapor," *Catal. Lett.*, **91** [1–2] 89–94 (2003).

[8]S. Rojanapipatkul and B. Jongsomjit, "Synthesis of Cobalt on Cobalt-Aluminate Via Solvothermal Method and its Catalytic Properties for Carbon Monoxide Hydrogenation," *Catal. Commun.*, **10**, 232–6 (2008).

[9]D. P. Jiang, Y. Q. Zou, L. B. Su, H. L. Tang, F. Wu, L. H. Zheng, H. J. Li, and J. Xu, "A Co^{2+}-Doped Mg$_{0.4}$Al$_{2.4}$O$_4$ Spinel Crystal as Saturable Absorber for a LD Pumped Er: Glass Microchip Laser at 1535 nm," *Laser Phys. Lett.*, **8**, 343–8 (2011).

[10]C. Wang and Z. Zhao, "Transparent MgAl2O4 Ceramic Produced by Spark-Plasma Sintering," *Scripta Mater.*, **61** [2] 193–6 (2009)

[11]L. Dussault, J. C. Dupin, C. Guimon, M. Monthioux, N. Latorre, T. Ubieto, E. Romero, C. Royo, and A. Monzon, "Development of Ni-Cu-Mg-Al Catalysts for the Synthesis of Carbon Nanofibers by Catalytic Decomposition of Methane," *J. Catal.*, **251**, 223–32 (2007).

[12]I. E. Achouri, N. Abatzoglou, C. Fauteux-Lefebvre, and N. Braidy, "Diesel Steam Reforming: Comparison of Two Nickel Aluminate Catalysts Prepared by Wet-Impregnation and Co-Precipitation," *Catal. Today*, **207**, 13–20 (2013).

[13]N. Bayal and P. Jeevanandam, "Synthesis of Metal Aluminate Nanoparticles by Sol-Gel Method and Studies on their Reactivity," *J. Alloy. Compd.*, **516**, 27–32 (2012).

[14]T. R. Hinklin, J. Azurdia, M. Kim, J. C. Marchal, S. Kumar, and R. M. Laine, "Finding Spinel in all the Wrong Places," *Adv. Mater.*, **20**, 1373–5 (2008).

[15]W. H. Bragg, "The Structure of the Spinel Group of Crystals," *Philos. Mag.*, **30** [176] 305–15 (1915).

[16]S. Nishikawa, "Structure of Some Crystals of the Spinel Group," *Proc. Math. Phys. Soc. Tokyo*, **8**, 199–209 (1915).

[17]K. E. Sickafus, J. M. Wills, and N. W. Grimes, "Spinel Compounds: Structure and Property Relations," *J. Am. Ceram. Soc.*, **82** [12] 3279–92 (1999).

[18]D. S. McClure, "The Distribution of Transition Metal Cations in Spinels," *J. Phys. Chem. Solids*, **3**, 311–7 (1957).

[19]J. K. Burdett, G. D. Price, and S. L. Price, "Role of the Crystal-Field Theory in Determining Structure of Spinels," *J. Am. Chem. Soc.*, **104**, 92–5 (1982).

[20]R. E. Carter, "Mechanism of Solid-State Reaction Between Magnesium Oxide and Aluminum Oxide and Between Magnesium Oxide and Ferric Oxide," *J. Am. Ceram. Soc.*, **44** [3] 116–20 (1961).

[21]P. H. Bolt, F. H. P. M. Habraken, and J. W. Geus, "Formation of Nickel, Cobalt, Copper, and Iron Aluminates From α- and γ-Alumina-Supported Oxides: A Comparative Study," *J. Solid State Chem.*, **135**, 59–69 (1998).

[22]J. M. Fernandez Colinas and C. Otero Arean, "Kinetics of Solid-State Spinel Formation: Effect of Cation Coordination Preference," *J. Solid State Chem.*, **109**, 43–6 (1994).

[23]T. Hinklin, B. Toury, C. Gervais, F. Babonneau, J. J. Gislason, R. W. Morton, and R. M. Laine, "Liquid-Feed Flame Spray Pyrolysis of Metalloorganic and Inorganic Alumina Sources in the Production of Nanoalumina Powders," *Chem. Mater.*, **16** [1] 21–30 (2003).

[24]C. R. Bickmore, K. F. Waldner, D. R. Treadwell, and R. M. Laine, "Ultrafine Spinel Powders by Flame Spray Pyrolysis of a Magnesium Aluminum Double Alkoxide," *J. Am. Ceram. Soc.*, **79** [5] 1419–23 (1996).

[25]R. M. Laine, R. Baranwal, T. Hinklin, D. Treadwell, A. Sutorik, C. Bickmore, K. Waldner, and S. S. Neo, "Making Nanosized Oxide Powders from Precursors by Flame Spray Pyrolysis"; pp. 17–24 in *Novel Synthetic and Processing Routes to Ceramics. Key Engineering Materials*, Vols 159–160, Edited by K. Uematsu and H. Otsuka. Trans Tech Publ. Ltd., Dürten, Switzerland, 1998.

[26]J. A. Azurdia, J. Marchal, P. Shea, H. Sun, X. Q. Pan, and R. M. Laine, "Liquid-Feed Flame Spray Pyrolysis as a Method of Producing Mixed-Metal Oxide Nanopowders of Potential Interest as Catalytic Materials. Nanopowders Along the NiO-Al2O3 Tie Line Including (NiO)$_{0.22}$(Al$_2$O$_3$)$_{0.78}$, a New Inverse Spinel Composition," *Chem. Mater.*, **18**, 731–9 (2006).

[27]J. Azurdia, J. Marchal, and R. M. Laine, "Synthesis and Characterization of Mixed-Metal Oxide Nanopowders Along the CoO$_x$–Al$_2$O$_3$ Tie Line Using Liquid-Feed Flame Spray Pyrolysis," *J. Am. Ceram. Soc.*, **89** [9] 2749–56 (2006).

[28]T. R. Hinklin and R. M. Laine, "Synthesis of Metastable Phases in the Magnesium Spinel-Aluminum System," *Chem. Mater.*, **20**, 553–8 (2008).

[29]J. Marchal, T. John, R. Baranwal, T. Hinklin, and R. M. Laine, "Yttrium Aluminum Garnet Nanopowders Produced by Liquid-Feed Flame Spray Pyrolysis (LF-FSP) of Metalloorganic Precursors," *Chem. Mater.*, **16**, 822–31 (2004).

[30]R. Baranwal, M. P. Villar, R. Garcia, and R. M. Laine, "Synthesis, Characterization, and Sintering Behavior of Nano-Mullite Powder and Powder Compacts," *J. Am. Ceram. Soc.*, **84** [5] 951–61 (2001).

[31]I. Levin and D. Brandon, "Metastable Alumina Polymorphs: Crystal Structures and Transition Sequences," *J. Am. Ceram. Soc.*, **81** [8] 1995–2012 (1998).

[32]C. M. Lieber, "Nanoscale Science and Technology: Building a Big Future from Small Things," *MRS Bull.*, **28** [7] 486–91 (2003).

[33]B. C. Lippens and J. H. De Boer, "Study of Phase Transformation During Calcination of Aluminum Hydroxides by Selected Area Electron Diffraction," *Acta Cryst.*, **17**, 1312–21 (1964).

[34]T. Hahn (Ed.), *International Tables of Crystallography*, Vol. A. Kluwer, London, UK. 1995.

[35]J. A. Ball, M. Pirzada, R. W. Grimes, M. O. Zacate, D. W. Price, and B. P. Uberuaga, "Predicting Lattice Parameter as a Function of Cation Disorder in MgAl$_2$O$_4$ Spinel," *J. Phys.: Condens. Matter*, **17**, 7621–31 (2005).

[36]A. Krell, K. Waetzig, and J. Klimke, "Influence of the Structure of MgO·NAl2O3 Spinel Lattices on Transparent Ceramics Processing and Properties," *J. Eur. Ceram. Soc.*, **32**, 2887–98 (2012).

[37]P. Bassoul and J. C. Gilles, "Structure and Microstructure of the Metastable B Phase (NiAl$_{10}$O$_{16}$): I. Preparation and Structural Study by X-ray Diffraction," *J. Solid State Chem.*, **58**, 383–8 (1985).

[38]P. Bassoul and J. C. Gilles, "Structure and Microstructure of the Metastable B Phase (NiAl$_{10}$O$_{16}$): II. An Electron Microscopic Investigation of the Microstructure," *J. Solid State Chem.*, **58**, 389–97 (1985).

[39]R. J. Bratton, "Initial Sintering Kinetics of MgAl$_2$O$_4$," *J. Am. Ceram. Soc.*, **52** [8] 417–9 (1969).

[40]M. Rubat du Merac, H.-J. Kleebe, M. M. Müller, and I. E. Reimanis, "Fifty Years of Research and Development Coming to Fruition; Unraveling the Complex Interactions During Processing of Transparent Magnesium Aluminate (MgAl$_2$O$_4$) Spinel," *J. Amer. Ceram. Soc.*, **96** [11] 3341–65 (2013)

[41]Y. M. Chiang and W. D. Kingery, "Grain-Boundary Migration in Nonstoichiometric Solid Solutions of Magnesium Aluminate Spinel: II, Effects of Grain-Boundary Nonstoichiometry," *J. Am. Ceram. Soc.*, **73** [5] 1153–8 (1990).

[42]S. T. Murphy, C. A. Gilbert, R. Smith, T. E. Mitchell, and R. W. Grimes, "Non-Stoichiometry in MgAl2O4 Spinel," *Phil. Mag.*, **90**, 1297–305 (2010).

[43]J. A. Ball, S. T. Murphy, R. W. Grimes, D. Bacorisen, R. Smith, B. P. Uberuaga, and K. E. Sickafus, "Defect Processes in MgAl$_2$O$_4$ Spinel," *Solid State Sci.*, **10**, 717–24 (2008).

[44]K. Mocala and A. Navrotsky, "Structural and Thermodynamic Variation in Nickel Aluminate Spinel," *J. Am. Ceram. Soc.*, **72** [5] 826–32 (1989).

[45]K. I. Lilova, A. Navrotsky, B. C. Melot, and R. Seshadri, "Thermodynamics of CoAl$_2$O$_4$–CoGa$_2$O$_4$ Solid Solutions," *J. Solid State Chem.*, **183**, 1266–71 (2010).   □